Electronic Supplementary Information (ESI)

Evolution of the solid electrolyte interphase enable by FeN_X/C catalysts for sodium-ion storage

Huicong Xia,[a,b] Lingxing Zan,[b,c] Gan Qu,[a] Yunchuan Tu,[b] Hongliang Dong,[d] Yifan Wei,[a] Kaixin Zhu,[b] Yue Yu,[a] Yongfeng Hu,[e] Dehui Deng,*[,b] and Jianan Zhang*[,a]

[a]*College of Materials Science and Engineering, Zhengzhou University, Zhengzhou 450001, P. R. China*

E-mail: zjn@zzu.edu.cn

[b]*State Key Laboratory of Catalysis, iChEM, Dalian Institute of Chemical Physics, Chinese Academy of Sciences, Dalian 116023, P. R. China*

E-mail: dhdeng@dicp.ac.cn

[c]*Key Laboratory of Chemical Reaction Engineering of Shaanxi Province, College of Chemistry & Chemical Engineering, Yan'an University, Yan'an 716000, P. R. China*

[d]*Center for High Pressure Science and Technology Advanced Research, Pudong, Shanghai 201203, P. R. China*

[e]*Canadian Light Source, 44 Innovation Boulevard Saskatoon, Saskatoon, SK, S7N 2V3 Canada*

Table of Contents

Chemicals:

All chemicals and reagents were used as received without any further purification. Melamine (99%), Polyvinylpyrrolidone (PVP), ferric nitrate nonahydrate (98%), 1-Methyl-2-pyrrolidinone (NMP), and hydrogen chloride (33%) were purchased from Innochem. Poly(vinylidene fluoride) (PVDF) was purchased from Sigma-aldrich. Cu foil and carbon black were purchased from Canrd Co., ltd. Deionized water (DI) (Millipore, 18MΩ cm) was used in all experiments.

Synthesis of FeN_X/C-T:

FeN_X/C-T was prepared via a high temperature pyrolysis method. All the operations were performed under Ar atmosphere. In a typical operation, 6g of PVP and 9 g of $Fe(NO_3)_3 \cdot 9H_2O$ were dissolved in DI water of 180 mL as the solutions for preparing FeN_X/C-T materials. After completely dissolution, these solutions were heated and stirred at 90 °C for 12h. The precipitant dried at 80 °C in an oven. This powder was calcined at different temperatures (600, 700, and 800 ^oC) for 1 h in a tubular furnace with a heating rate of 2°C min^{-1} under a constant Ar flow. Afterwards, the samples were dissolved in 2 mol L^{-1} HCl, and the solutions were heated and stirred at 105 °C for 24h. A dark product was obtained by centrifugation, washing three times with DI water, and drying at 60 ^oC for 12 h and designated as FeN_X/C-T (FeN_X/C-600, FeN_X/C-700. and FeN_X/C-800).

Synthesis of N-C:

N-C was also prepared via a high temperature pyrolysis method. Typically, 6 g of PVP and 1 g of Melamine were dissolved together in DI of 180 mL. Then the solutions were heated and stirred at 90 °C for 12h. The precipitant dried at 80 °C in an oven. This powder was calcined at 700 ^oC for 1 h in a tubular furnace with a heating rate of 2 °C min^{-1} under a constant Ar flow and designated as N-C.

Characterizations:

Scanning electron microscopy (SEM) was performed on Hitachi S5500. Transmission electron microscopy (TEM), higher resolution TEM (HRTEM) analyses were conducted with a Tecnai G2 F20 microscope operated at an accelerating voltage of 200 kV. The highangle annular dark-field scanning transmission electron microscopy (HAADF-STEM) and corresponding energy-dispersive X-ray (EDX) mapping were carried out on a FEI Talos F200S microscope operated at an accelerating voltage of 200 kV. Atomic resolution HAADF STEM images were obtained by using a JEM-ARM 200F microscope, equipped with a probe-forming aberration corrector and operated at 200 kV. The powder X-ray diffraction (XRD) measurements were performed on a Rigaku SmartLab diffractometer with Cu Kα radiation (λ = 1.5406 Å) at 40 kV and 40 mA. Raman spectra were taken on a LabRam HR Evolution Raman system by using the 532 nm excitation laser at a power of about 0.3 mW. Nitrogen adsorption–desorption isotherms were measured on a Micromeritics ASAP 2460, where the Brunauer–Emmett–Teller (BET) and density functional theory (DFT) methods were used to characterize the specific surface areas and pore size distribution. The X-ray photoelectron spectrum (XPS) was performed on the Thermo Scientific K-Alpha system used Al Kα X-rays (hv = 1486.6 eV) as the excitation source. The binding energy (BE) values were calibrated using C 1s at 284.8 eV. The actual Fe loadings on sample were characterized by inductively coupled plasma optical emission spectroscopy (ICP-OES, PerkinElmer 8300). The measurements of X-ray absorption spectroscopy (XAS) at the Fe K-edge containing the X-ray absorption nearedge structure (XANES) and extended X-ray absorption fine structure (EXAFS) were performed at the beamline BL14W1 of Shanghai Synchrotron Radiation Facility (SSRF), China. The ^{57}Fe Mössbauer measurements were performed using a conventional spectrometer (Topologic Systems, Inc. MFD-500AV-02) in transmission geometry with constant acceleration mode.

Electrocatalytic measurement:

The FeN_X/C-T sample was directly punched as the anodes of SIBs. The electrochemical performance was evaluated using standard 2032-type coin cells, which were assembled by using the FeNX/C-T as anode material, a Na foil as the cathode, a glass fiber as the separator (Whatman GF/D), and 1.0M NaPF6 in EC:DEC = 1:1 Vol% as the electrolyte. The cell assembly was carried out in an Ar-filled glovebox (MBRAUN MB-Labstar Pro) with the concentrations of moisture and oxygen below 0.5 ppm. The charge and discharge cycling performance, rate performance and galvanostatic intermittent titration technique (GITT) were measured by the NEWARE Battery Testing System with a voltage range of 0.01-3.0 V at room temperature. Cyclic voltammetry (CV) and electrochemical impedance spectra (EIS) measurements were implemented by CHI electrochemical workstation.

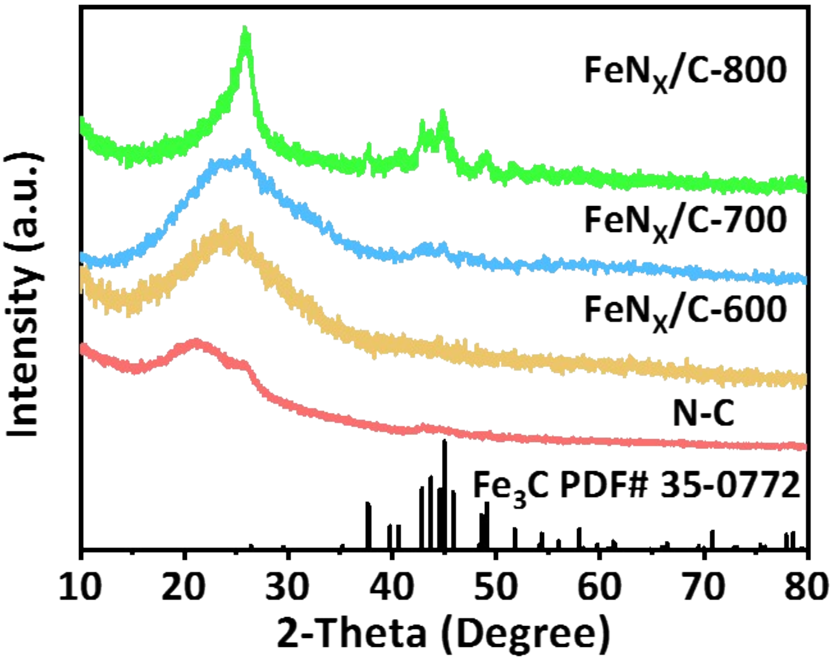

Figure S1. XRD patterns of the N-C, FeN$_X$/C-600, FeN$_X$/C-700, and FeN$_X$/C-800.

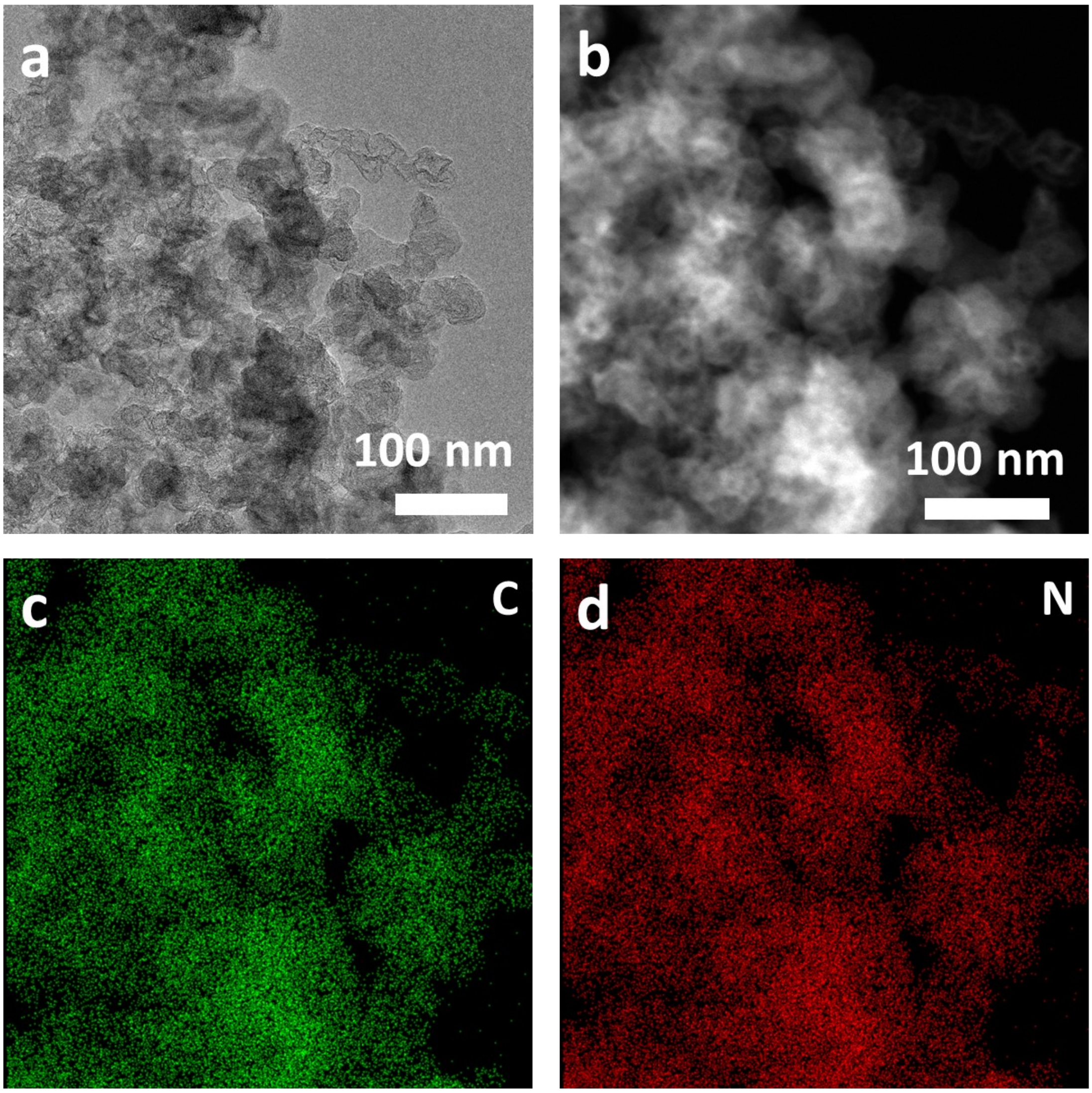

Figure S2. a) TEM images and b-d) EDS-element mapping of the N-C.

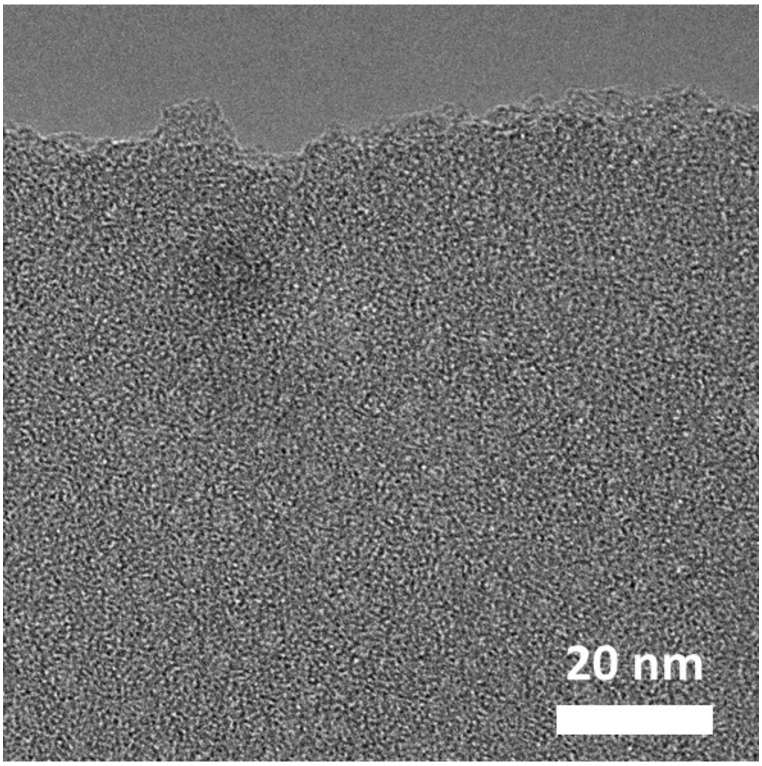

Figure S3. TEM image of FeN_X/C-600

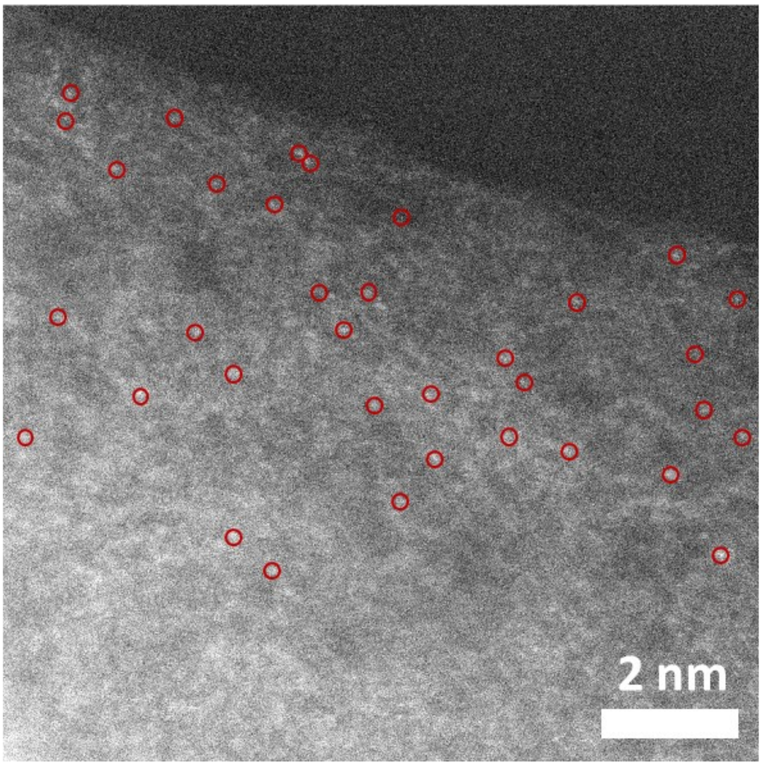

Figure S4. HAADF-STEM image of FeN_X/C-700.

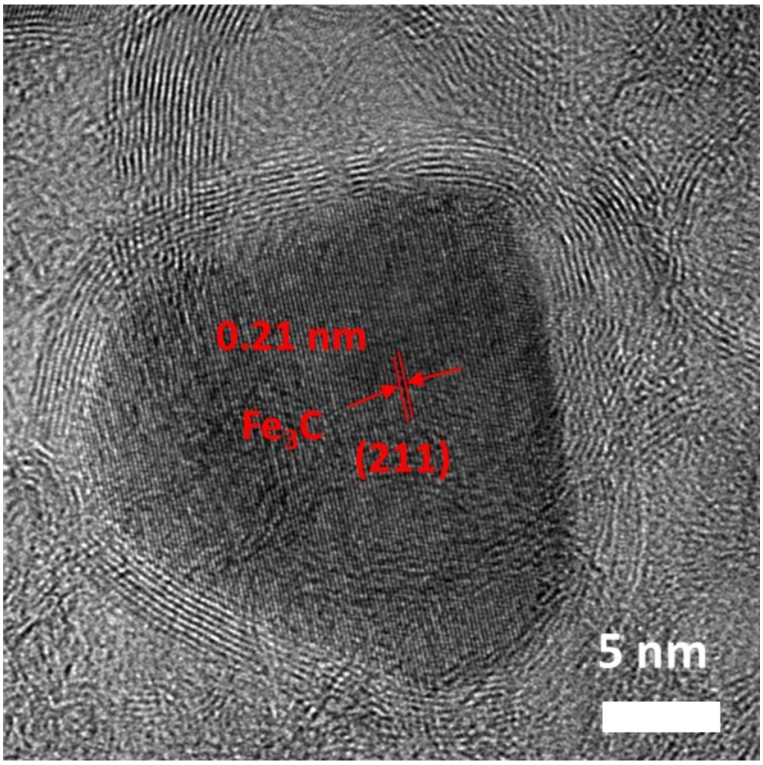

Figure S5. HRTEM image of FeN_X/C-800.

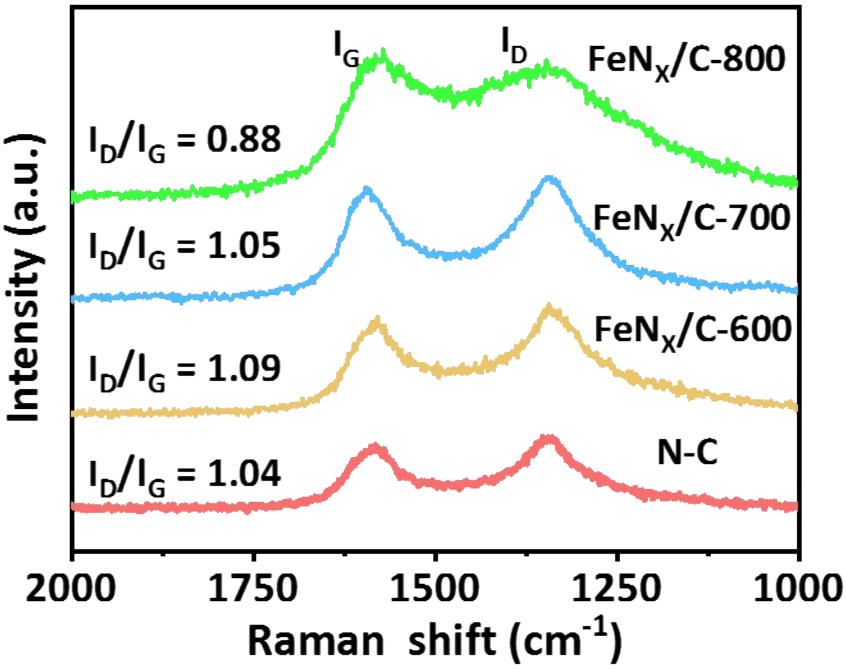

Figure S6. Raman spectra of the N-C, FeN_X/C-600, FeN_X/C-700, and FeN_X/C-800.

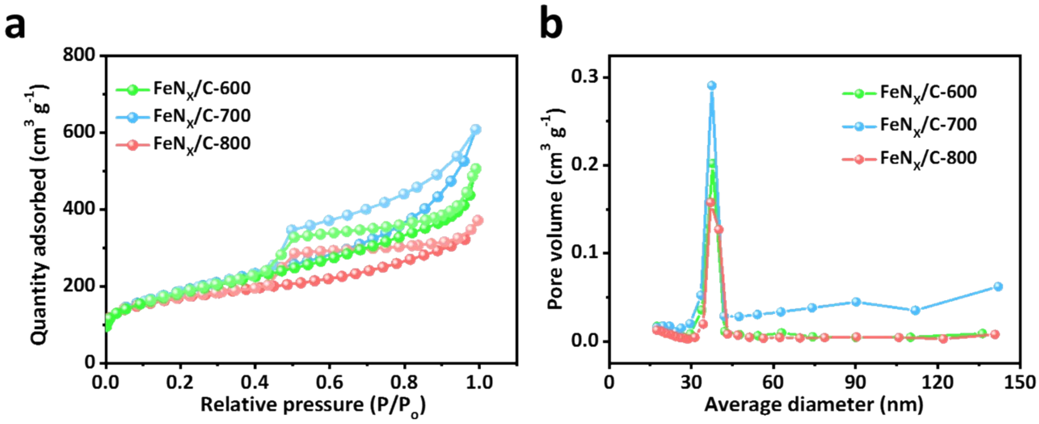

Figure S7. a) N2 adsorption−desorption isotherms and b) pore-size distribution curves of the FeN_X/C-600, FeN_X/C-700, and FeN_X/C-800, respectively.

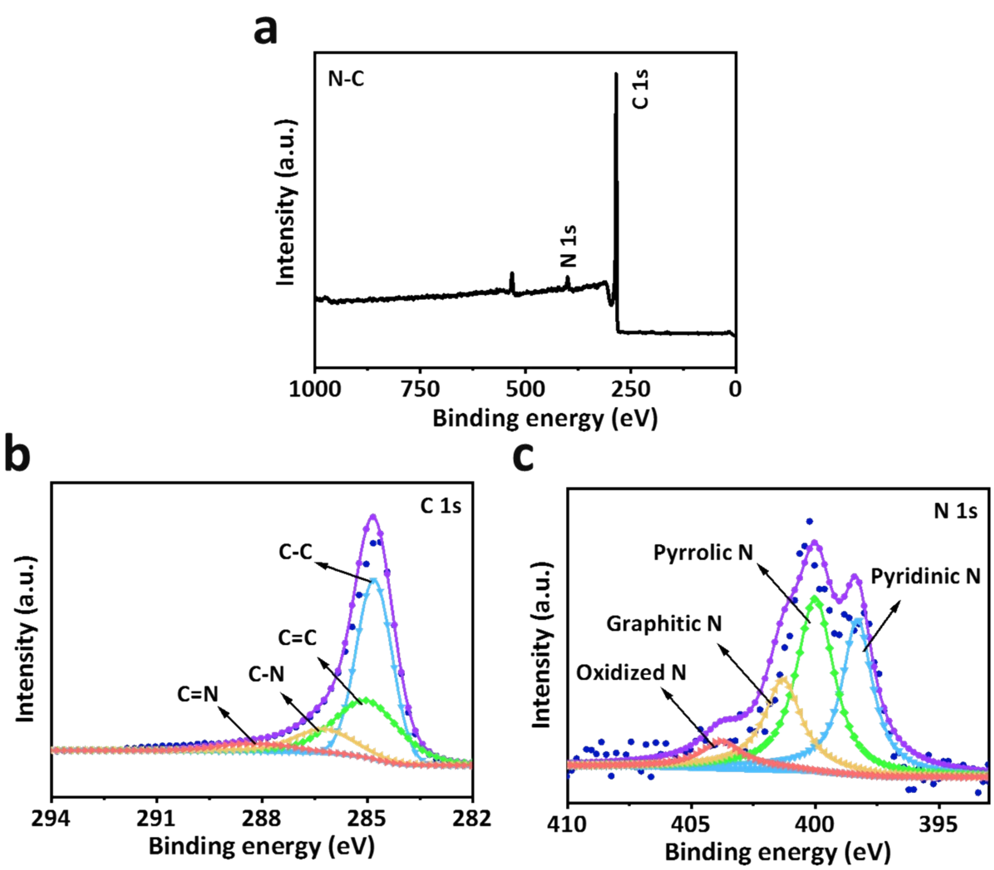

Figure S8. a) XPS survey scan of N-C. High-resolution b) C 1s and c) N 1s spectra, respectively.

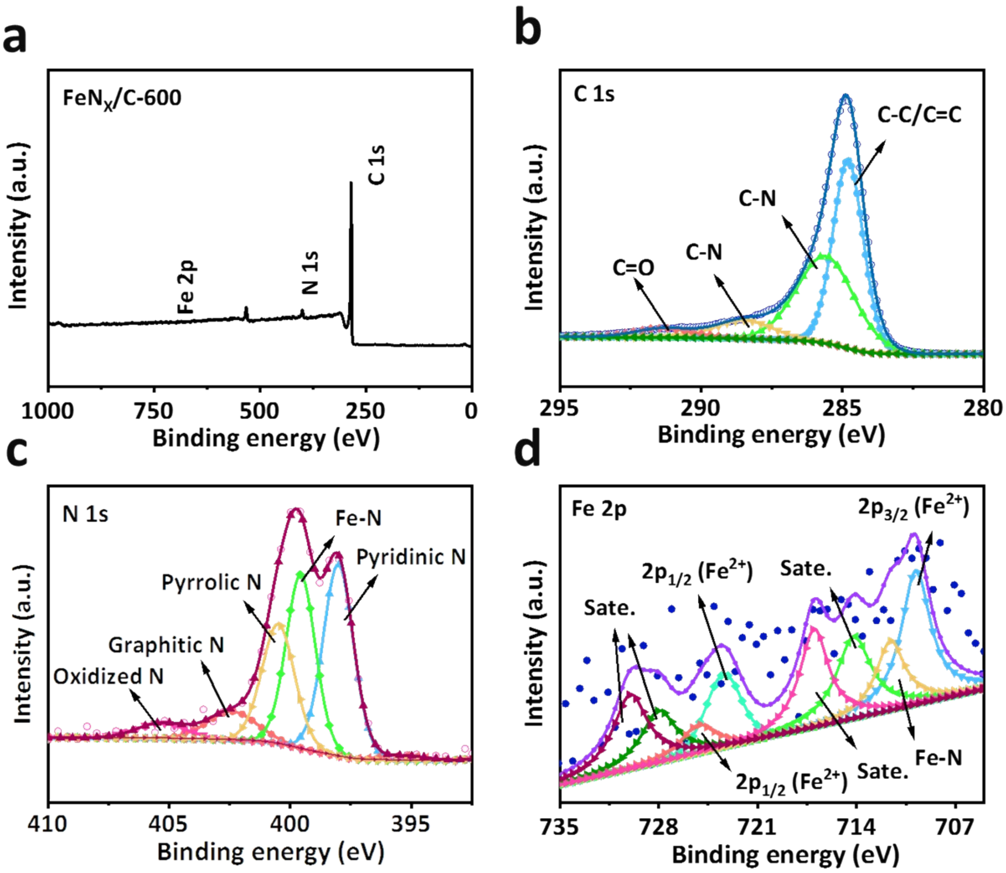

Figure S9. a) XPS survey scan of FeN$_X$/C-600. High-resolution b) C 1s, c) N 1s, and d) Fe 2p spectra, respectively.

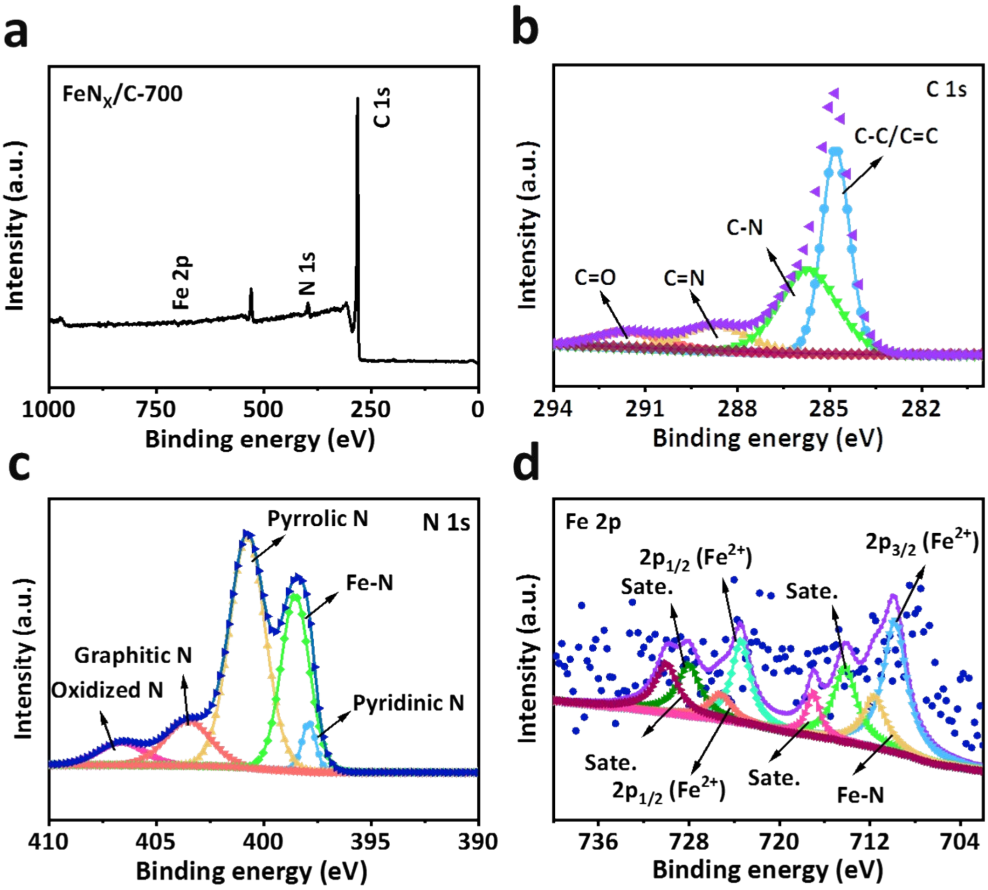

Figure S10. a) XPS survey scan of FeN$_X$/C-700. High-resolution b) C 1s, c) N 1s, and d) Fe 2p spectra, respectively.

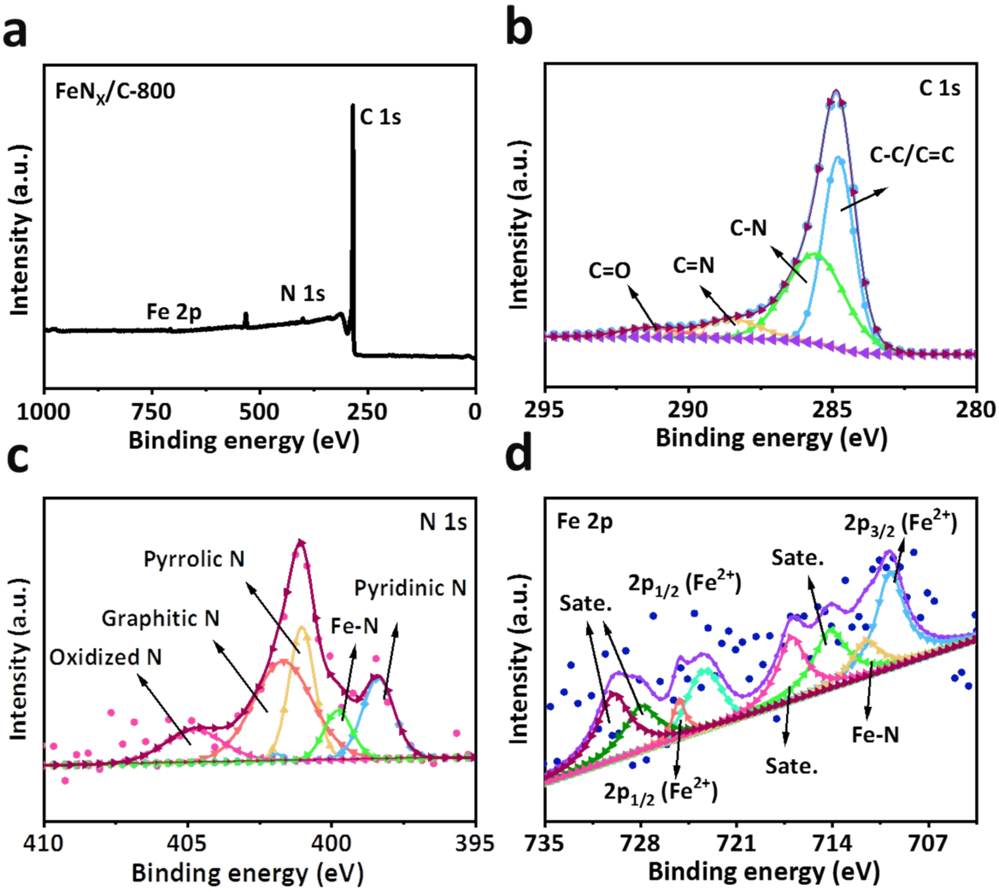

Figure S11. a) XPS survey scan of FeN_X/C-800. High-resolution b) C 1s, c) N 1s, and d) Fe 2p spectra, respectively.

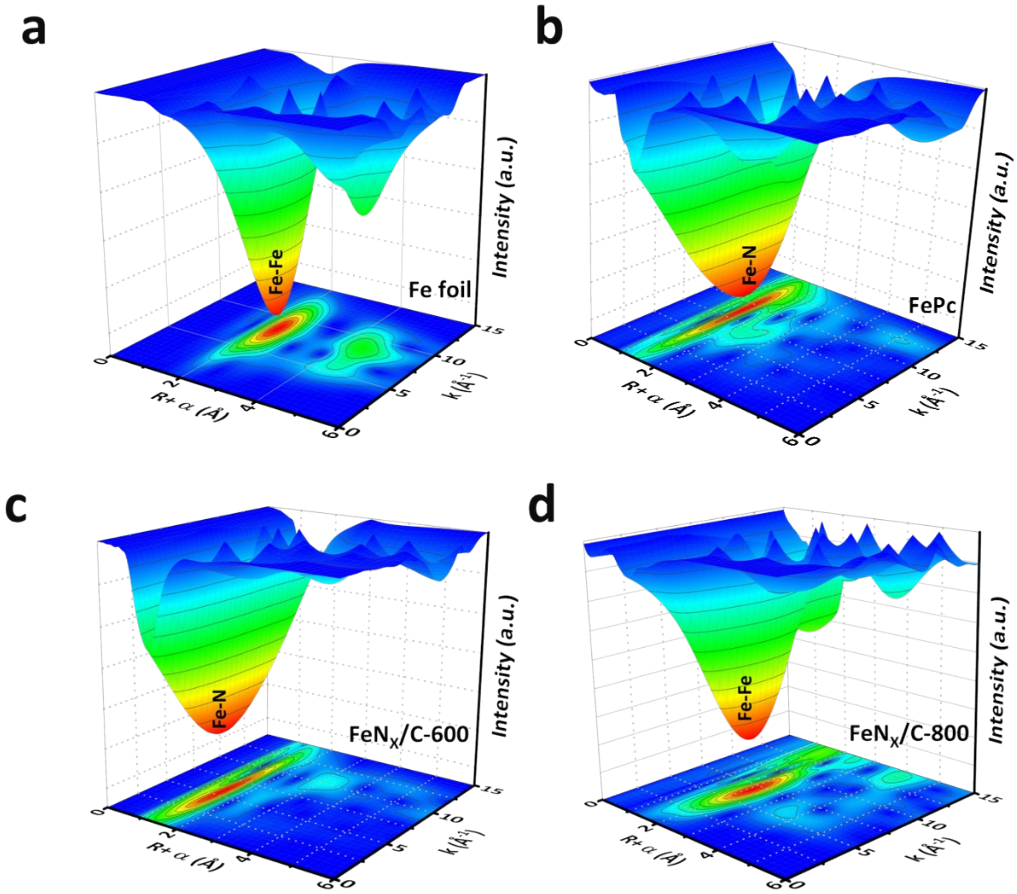

Figure S12. Wavelet transform of the k^3-weighted EXAFS data of Fe foil, FePc, FeN_X/C-600, and FeN_X/C-800.

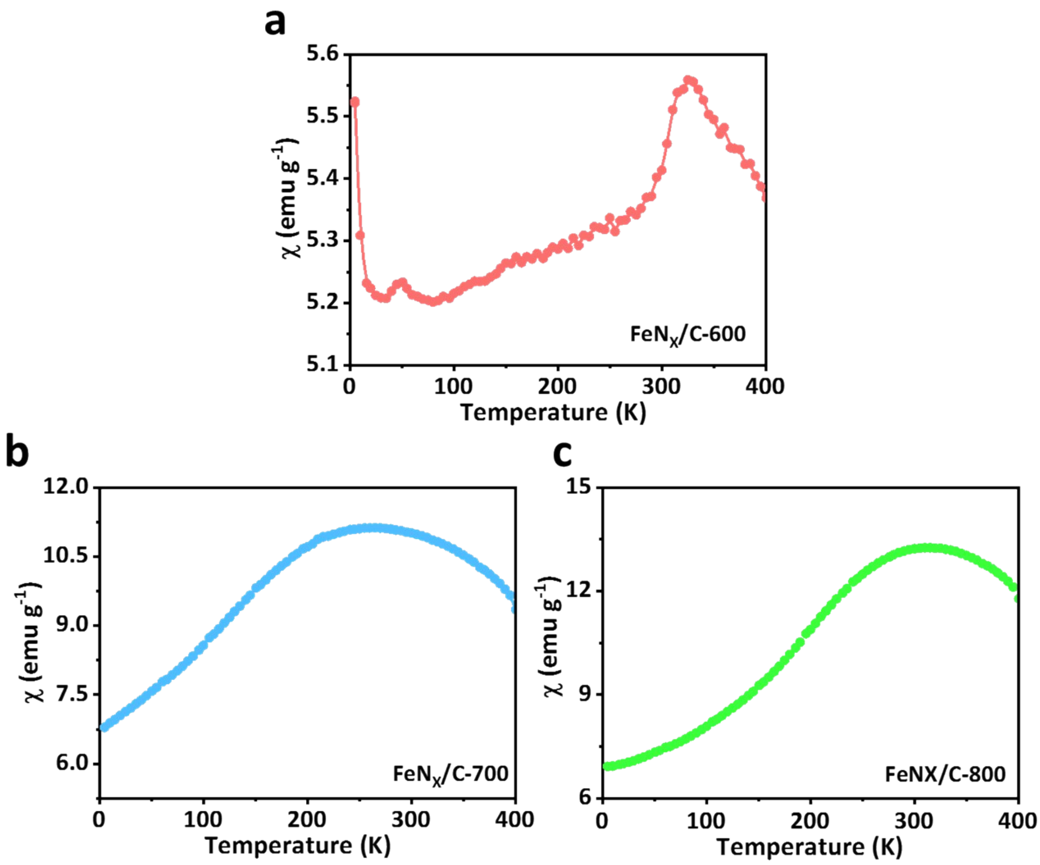

Figure S13. Magnetic susceptibility of a) FeN_X/C-600, b) FeN_X/C-700, and c) FeN_X/C-800, respectively.

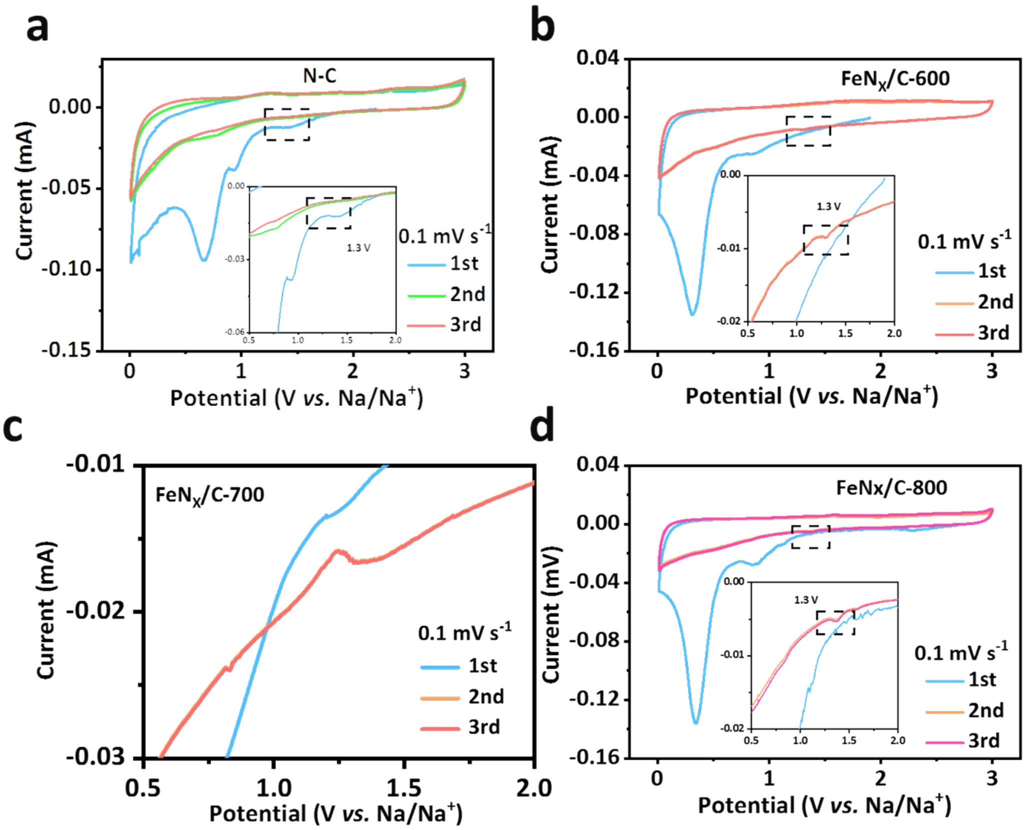

Figure S14. CV curves of the a) N-C, b) FeN$_X$/C-600, c) FeN$_X$/C-700, and d) FeN$_X$/C-800 between 0.01 and 3.0 V at a scanning rate of 0.1 mV s^{-1} at the first three cycles, respectively.

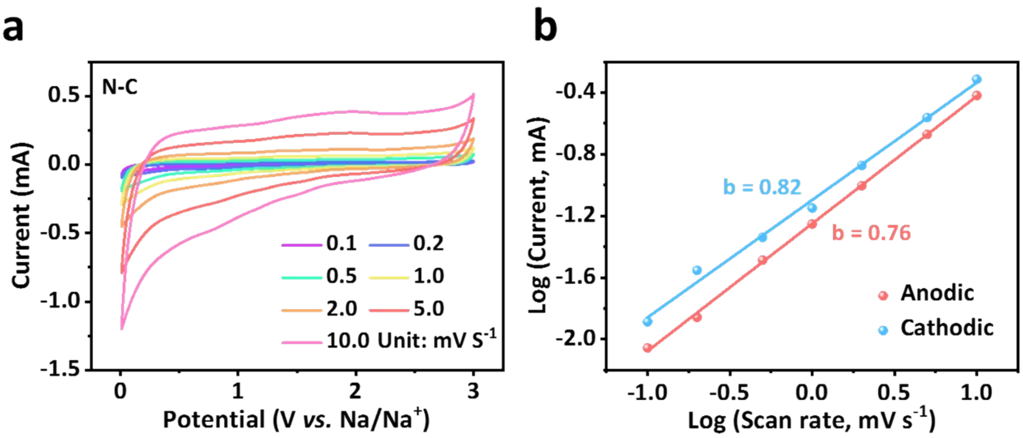

Figure S15. CV curves at various scan rates and (d) relationship between log(i) vs. log(n) for the N-C anode

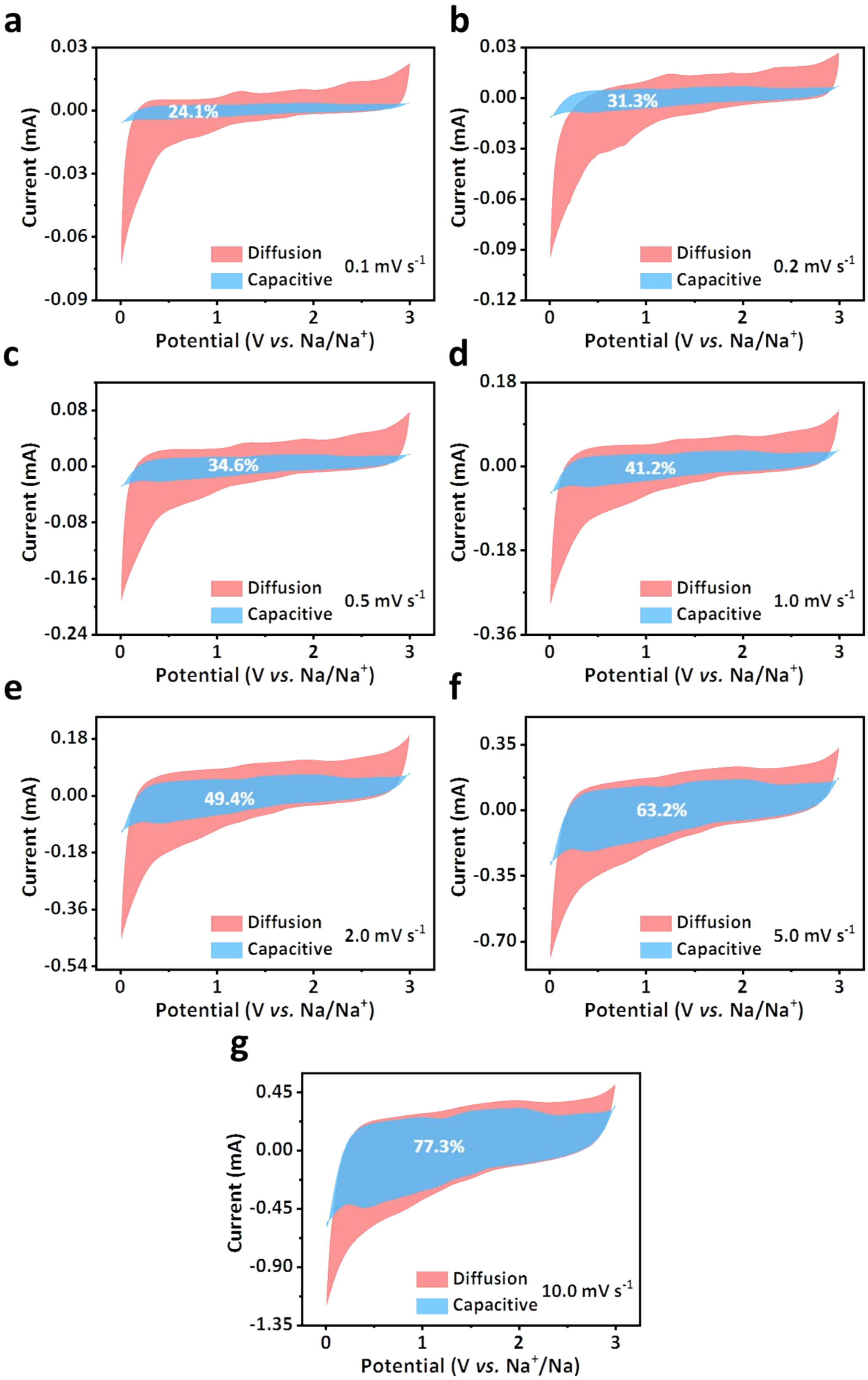

Figure S16. Capacitive-controlled and diffusion-controlled contributions at different scan rates of N-C.

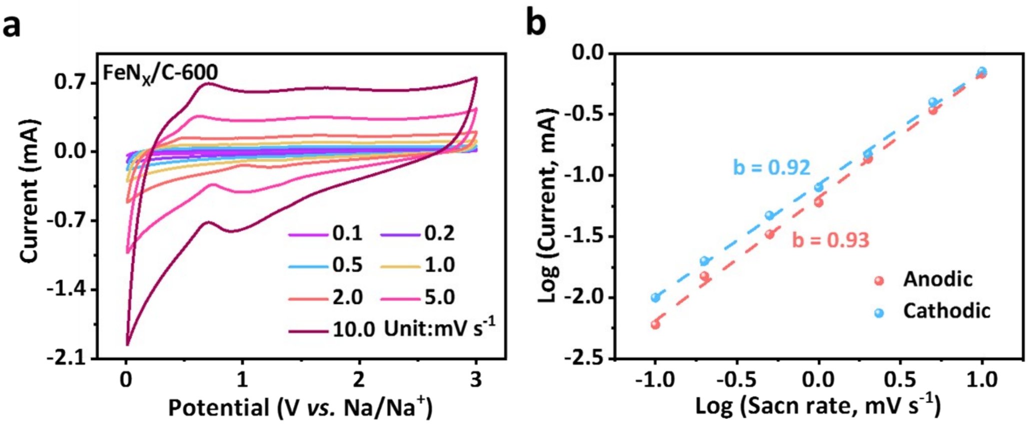

Figure S17. CV curves at various scan rates and (d) relationship between log(i) vs. log(n) for the FeN$_X$/C-600 anode.

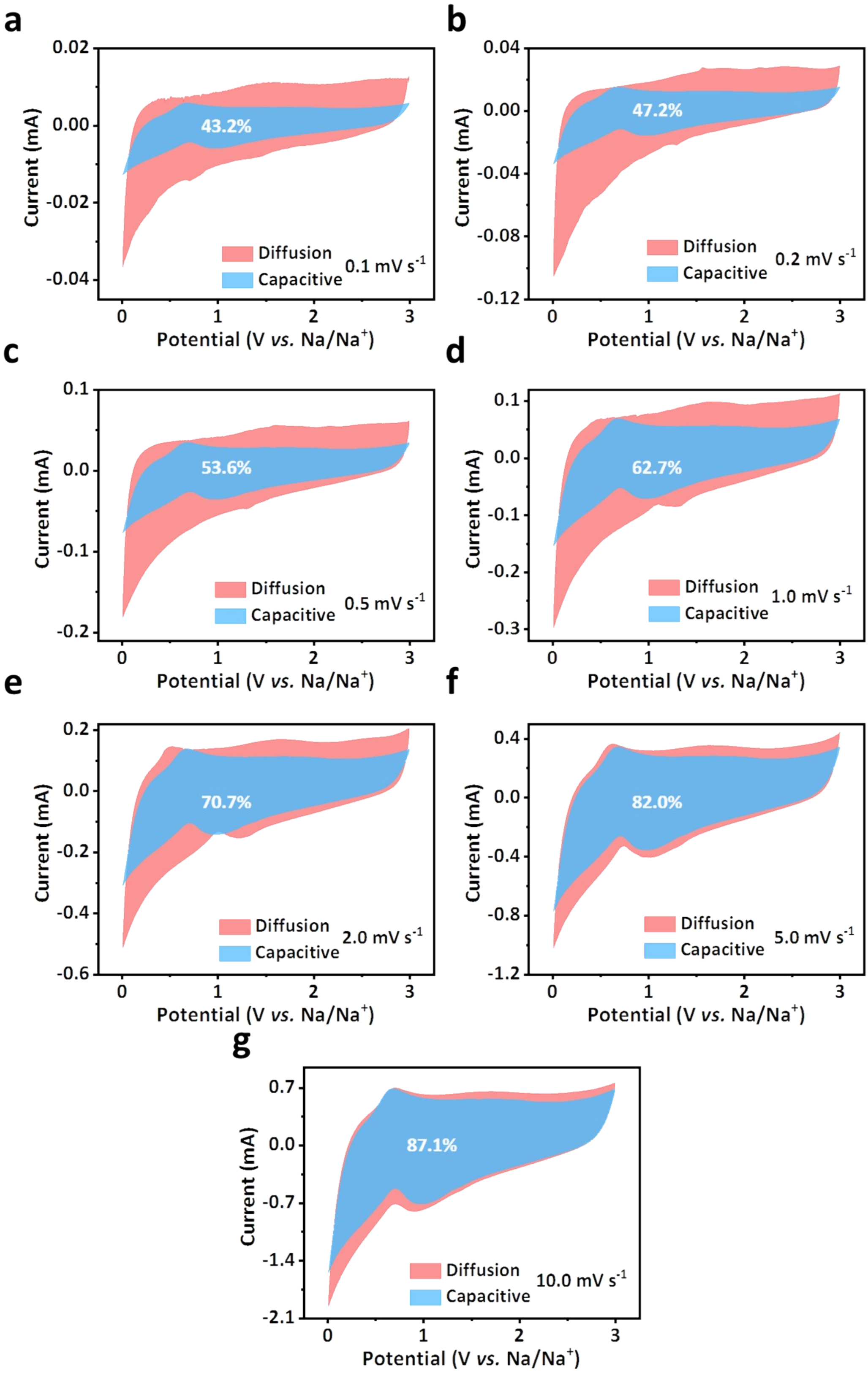

Figure S18. Capacitive-controlled and diffusion-controlled contributions at different scan rates of FeN_X/C-600.

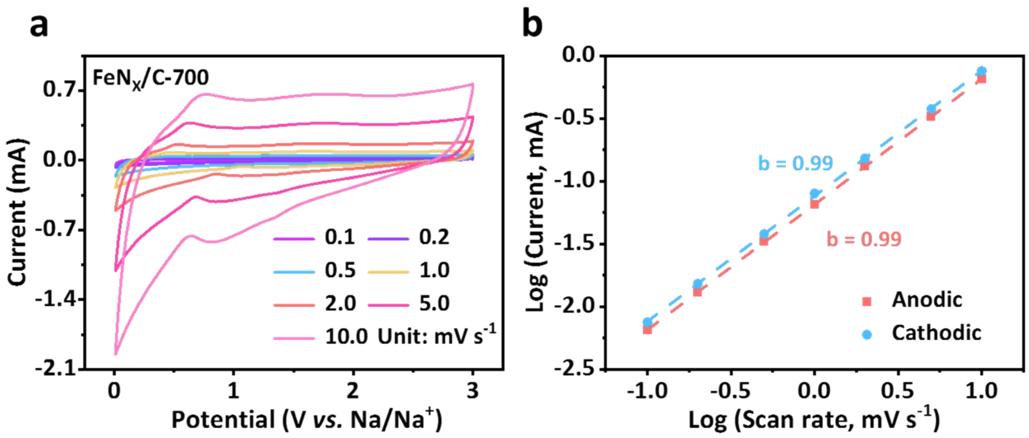

Figure S19. CV curves at various scan rates and (d) relationship between log(i) vs. log(n) for the FeN$_X$/C-700 anode.

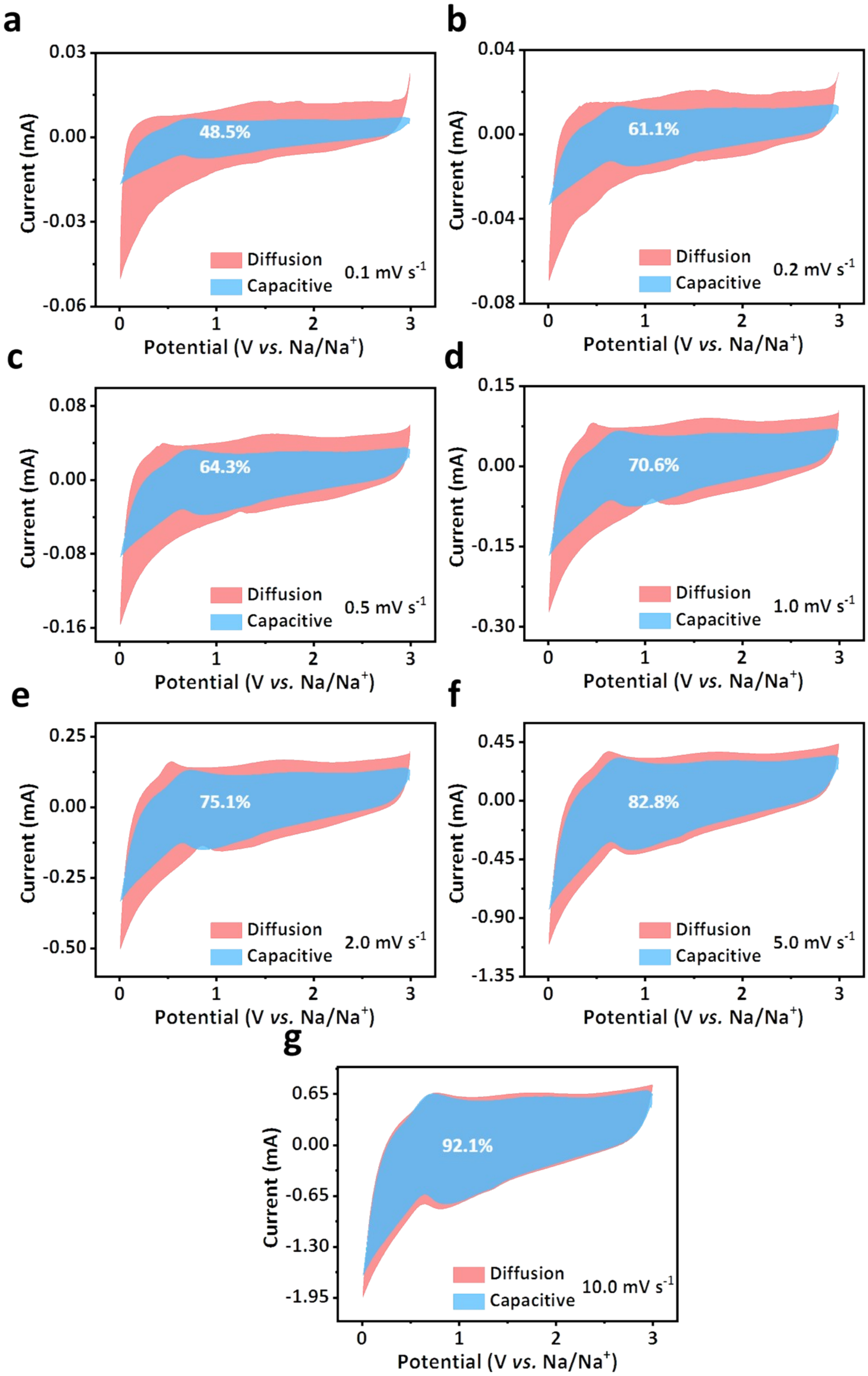

Figure S20. Capacitive-controlled and diffusion-controlled contributions at different scan rates of FeN_X/C-700.

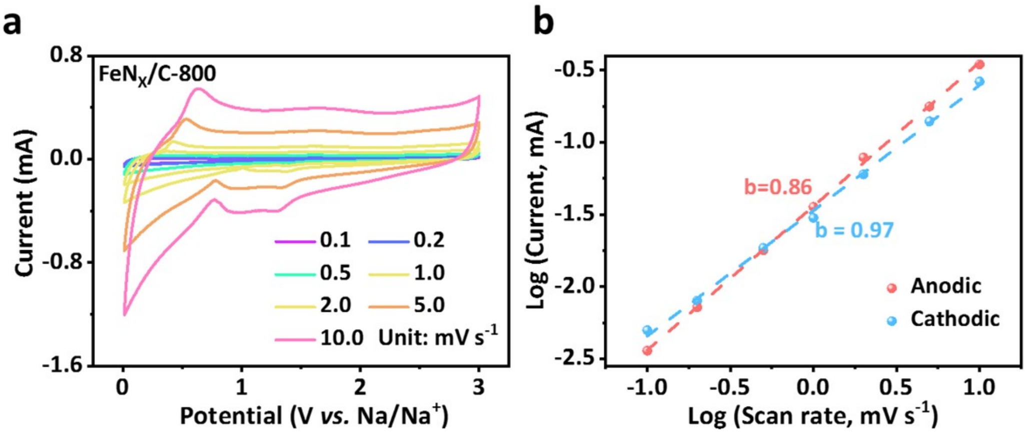

Figure S21. CV curves at various scan rates and (d) relationship between log(i) vs. log(n) for the FeN_X/C-800 anode.

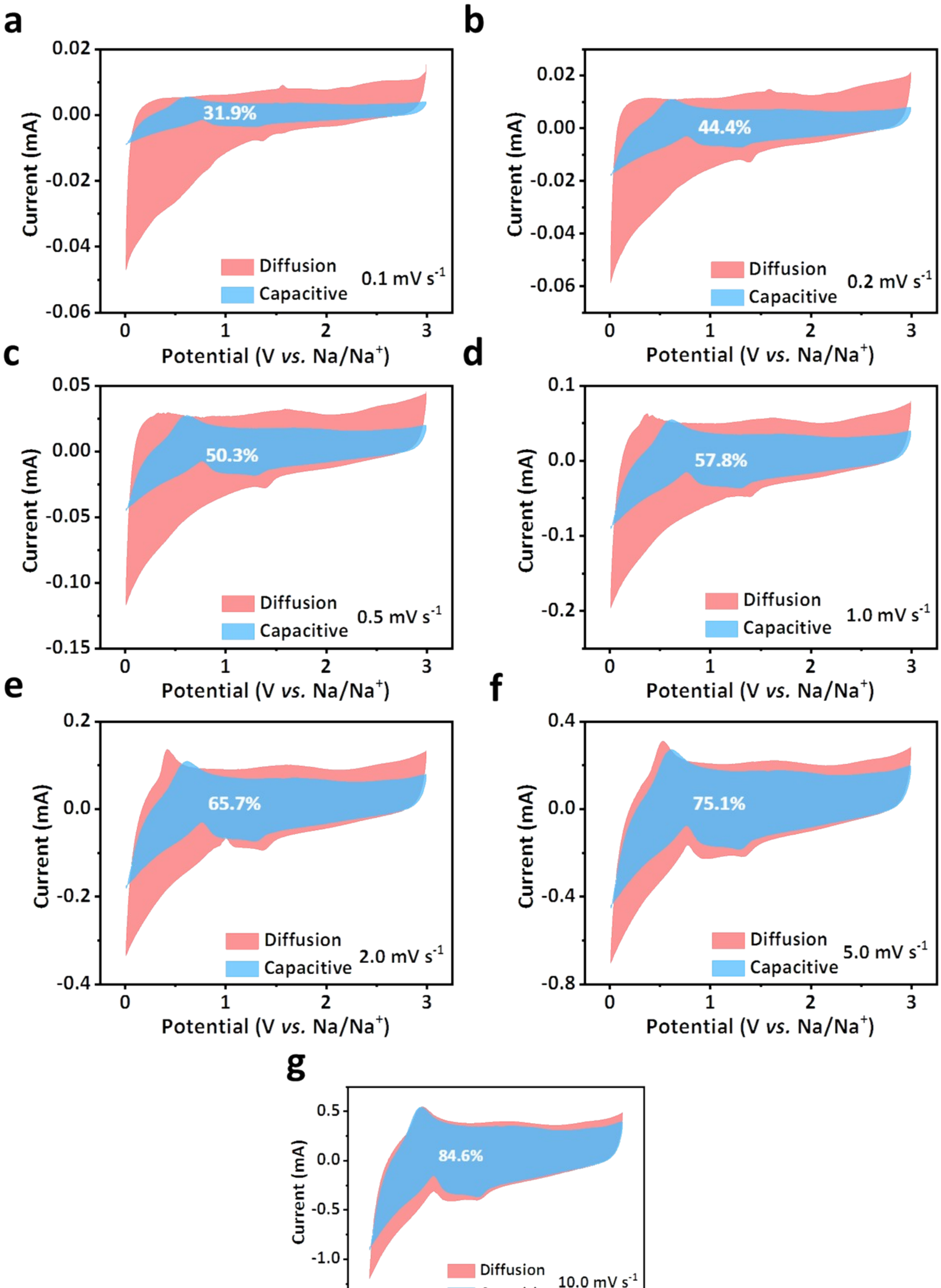

Figure S22. Capacitive-controlled and diffusion-controlled contributions at different scan rates of FeN_X/C-800.

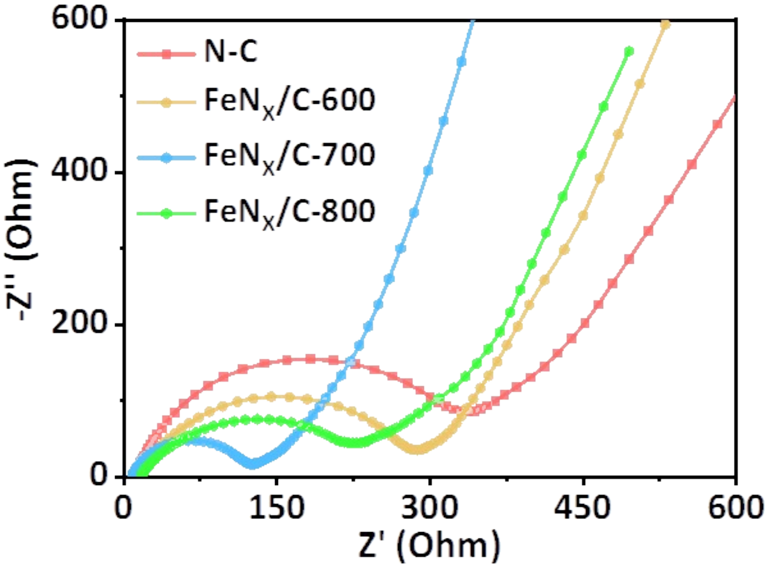

Figure S23. Nyquist plots of the N-C, FeN_X/C-600, FeN_X/C-700, and FeN_X/C-800.

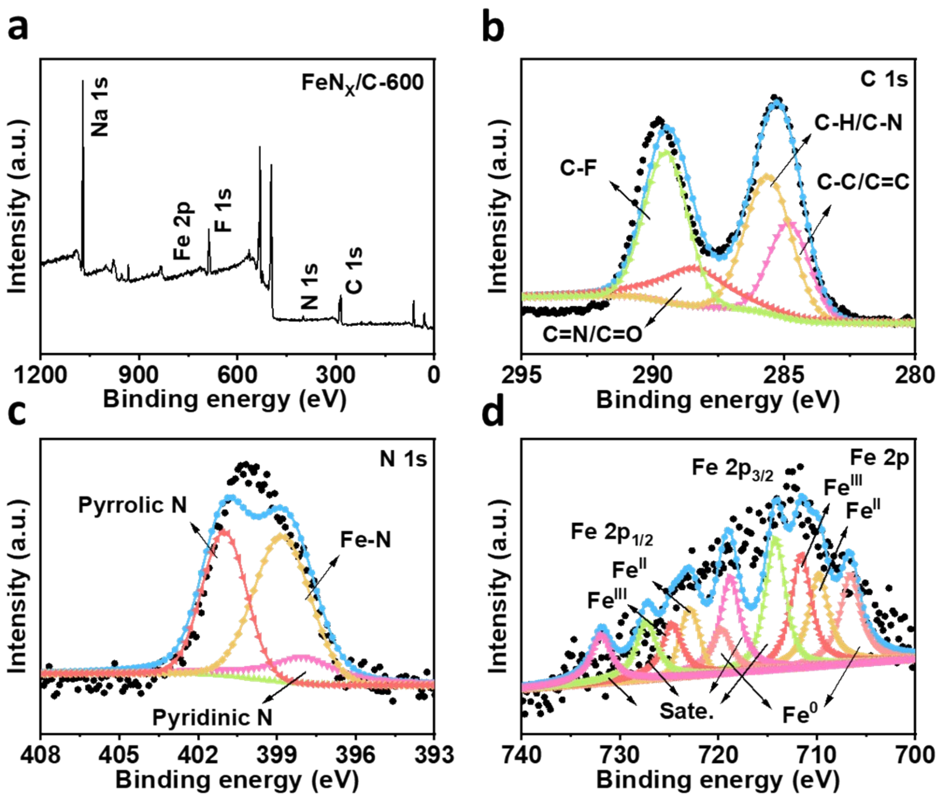

Figure S24 a) XPS full spectra and high-resolution b) C 1s, c) N 1s, and d) Fe 2p spectra of FeNX/C-600 after long-term cycles.

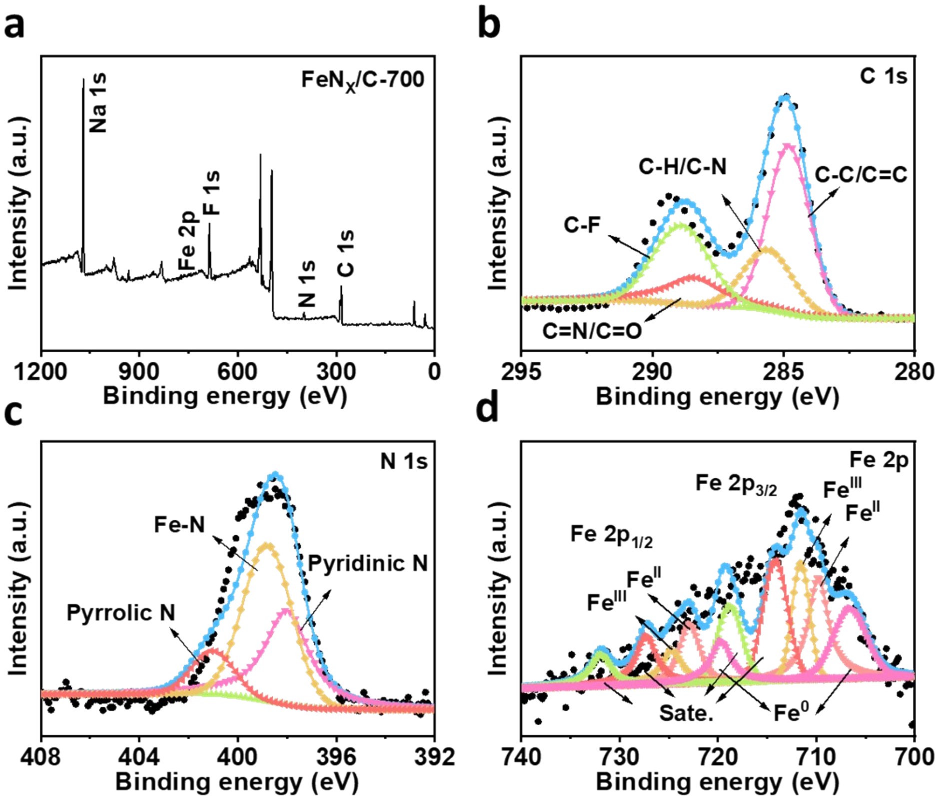

Figure S25 a) XPS full spectra and high-resolution b) C 1s, c) N 1s, and d) Fe 2p spectra of FeNX/C-700 after long-term cycles.

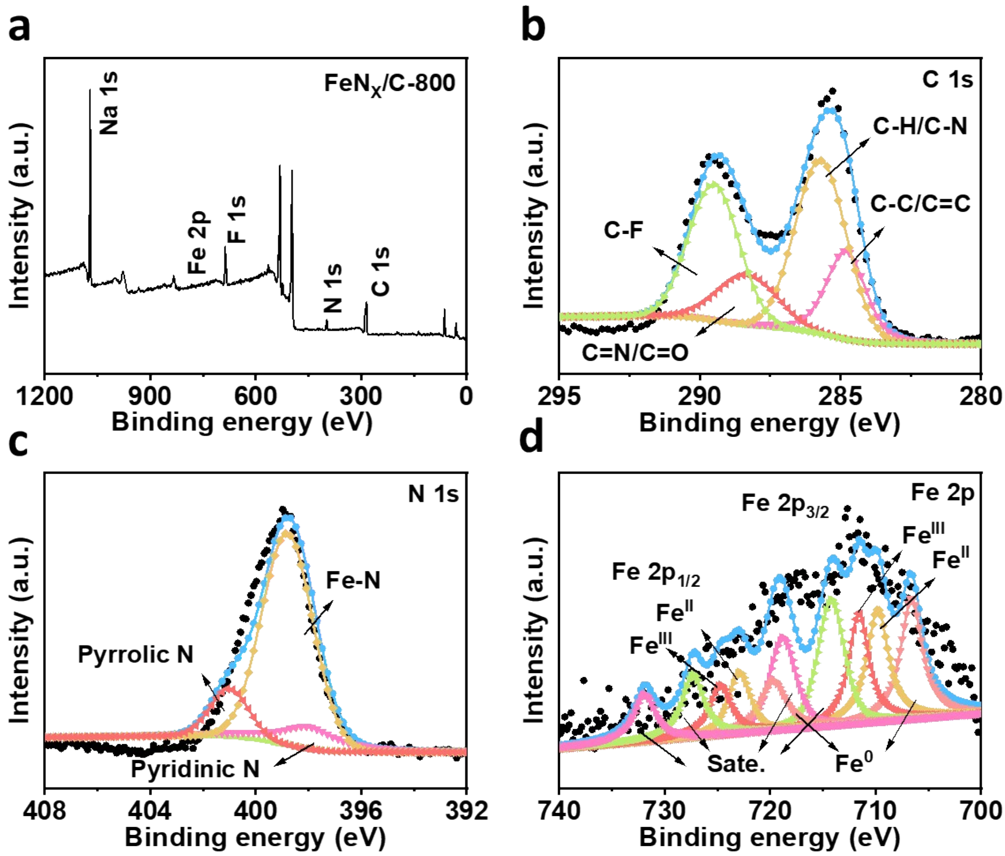

Figure S26 a) XPS full spectra and high-resolution b) C 1s, c) N 1s, and d) Fe 2p spectra of FeNX/C-800 after long-term cycles.

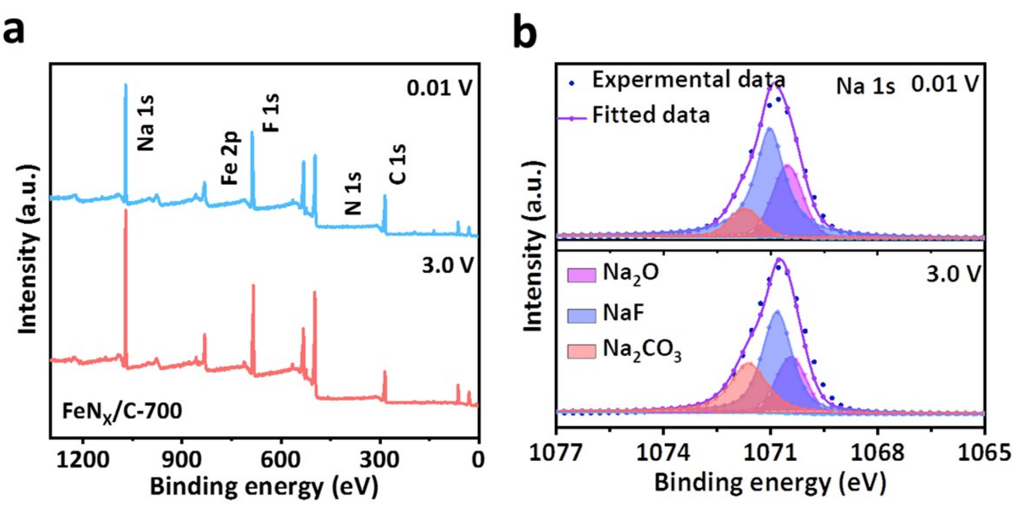

Figure S27. a) XPS full spectra and b) high-resolution Na 1s spectra of FeN_X/C-700 at different discharge/charge states

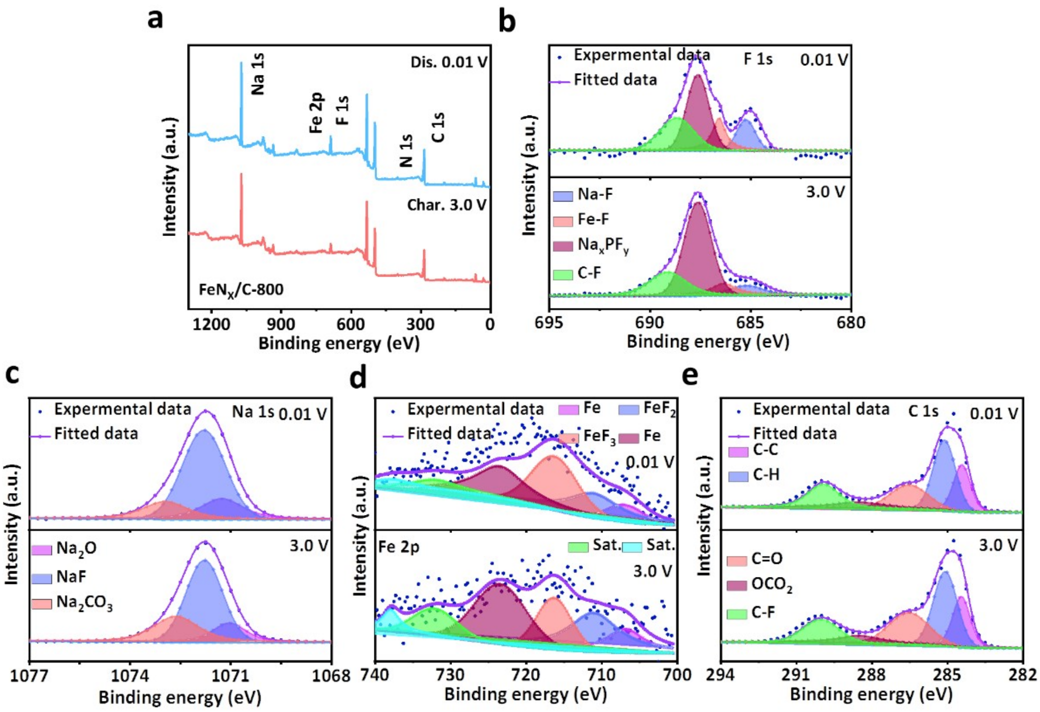

Figure S28. a) XPS full spectra and high-resolution b) F 1s, c) Na 1s, d) Fe 2p, and e) C 1s spectra of FeN$_X$/C-600 at different discharge/charge states

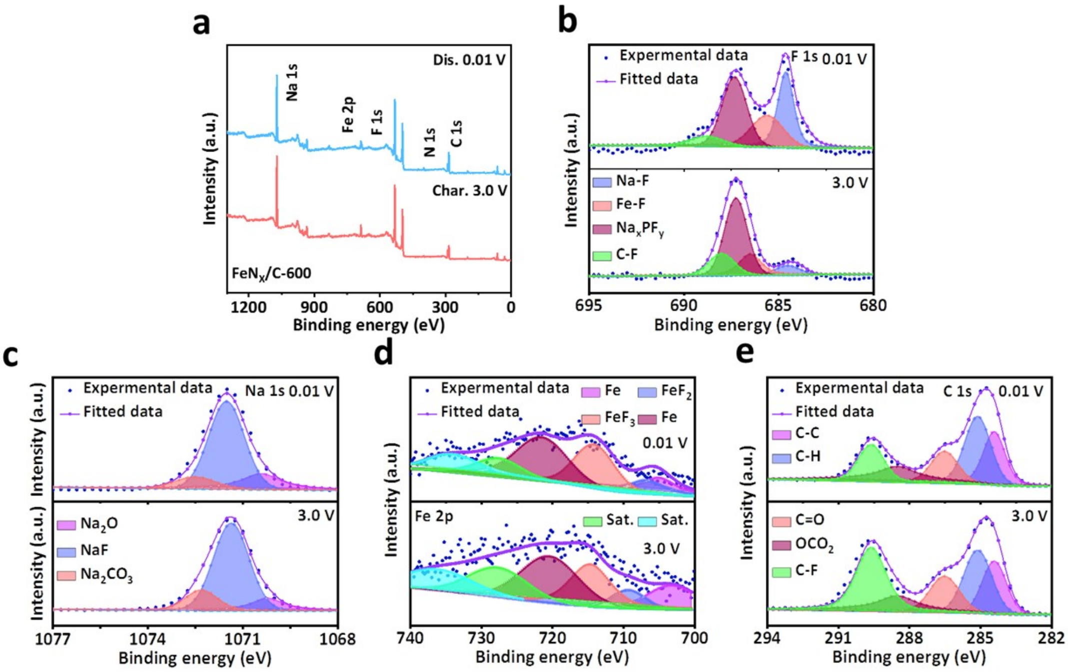

Figure S29. a) XPS full spectra and high-resolution b) F 1s, c) Na 1s, d) Fe 2p, and e) C 1s spectra of FeN$_X$/C-800 at different discharge/charge states

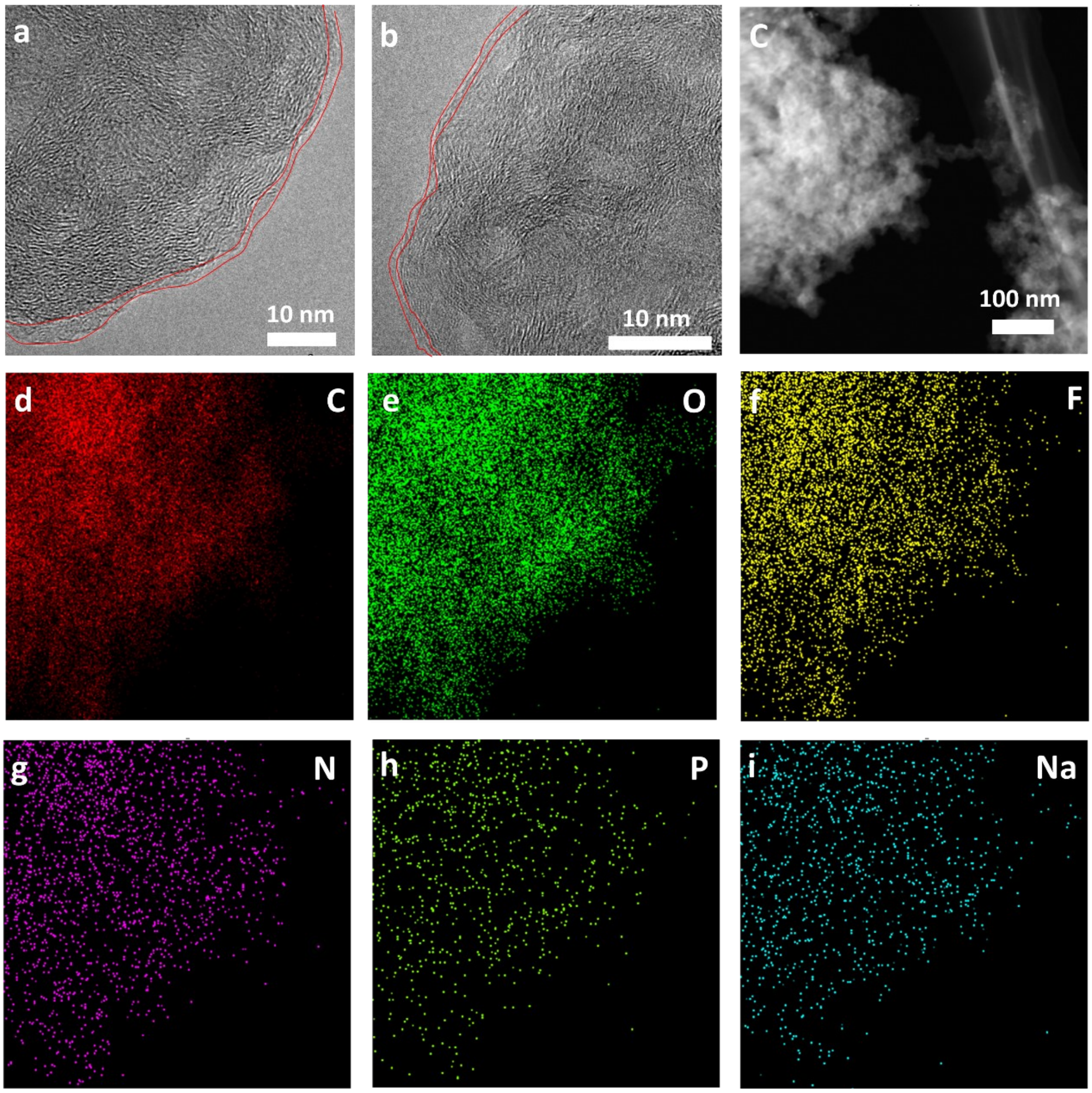

Figure S30. Morphological characterizations of SEI layers, HRTEM images of N-C after 10 cycles. STEM image of SEI layer of N-C, EDS-elemental maps of C, N, O, F, P, and Na.

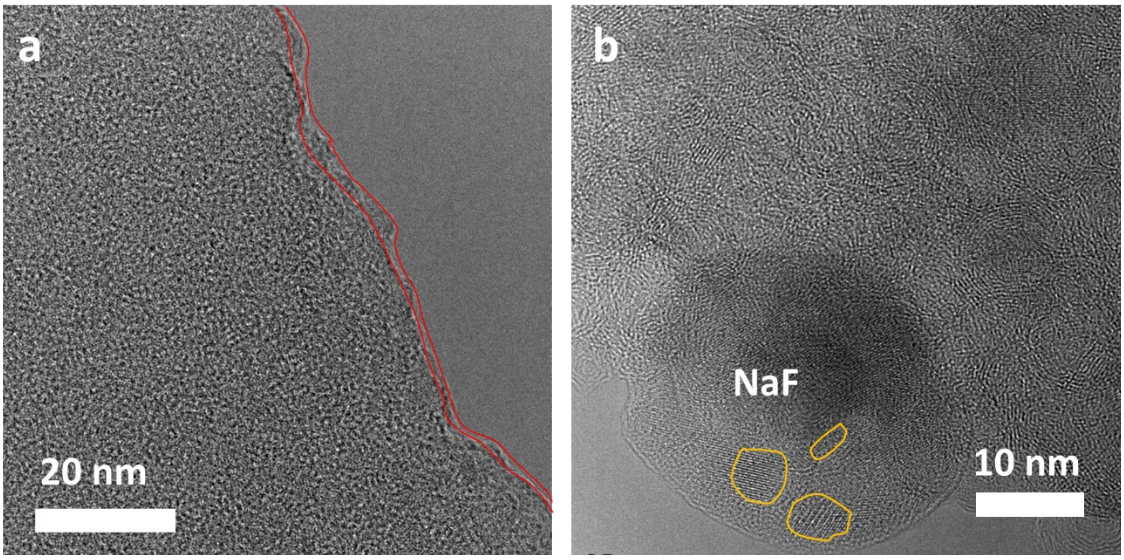

Figure S31. Morphological characterizations of SEI layers, TEM images of FeN_X/C-600 after 10 cycles.

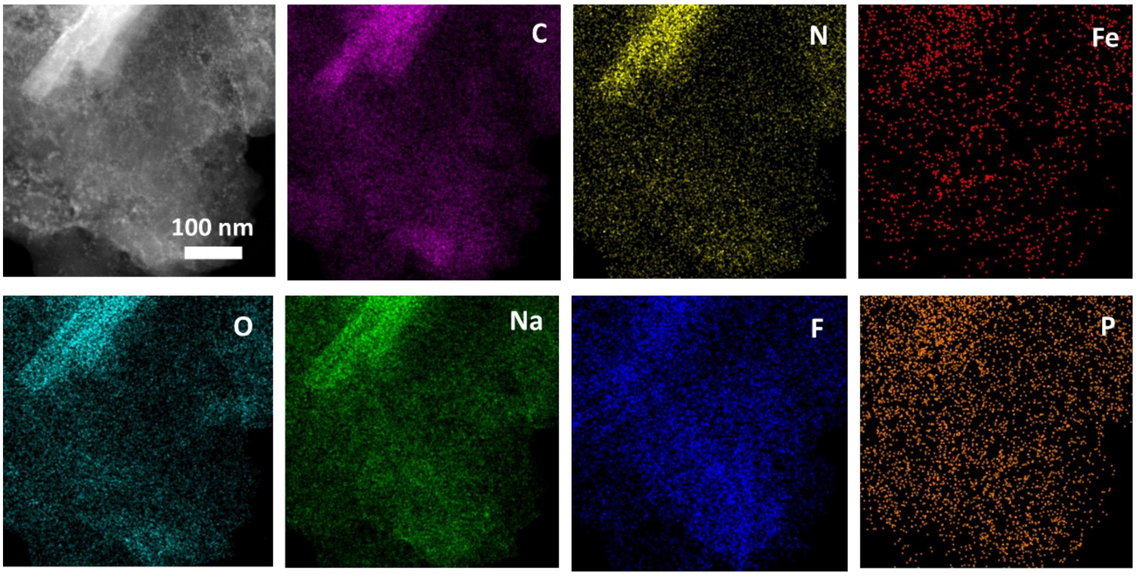

Figure S32. STEM image of SEI layer of $FeN_{X/}$C-600 EDS-elemental maps of C, N, Fe, O, Na, F, and P.

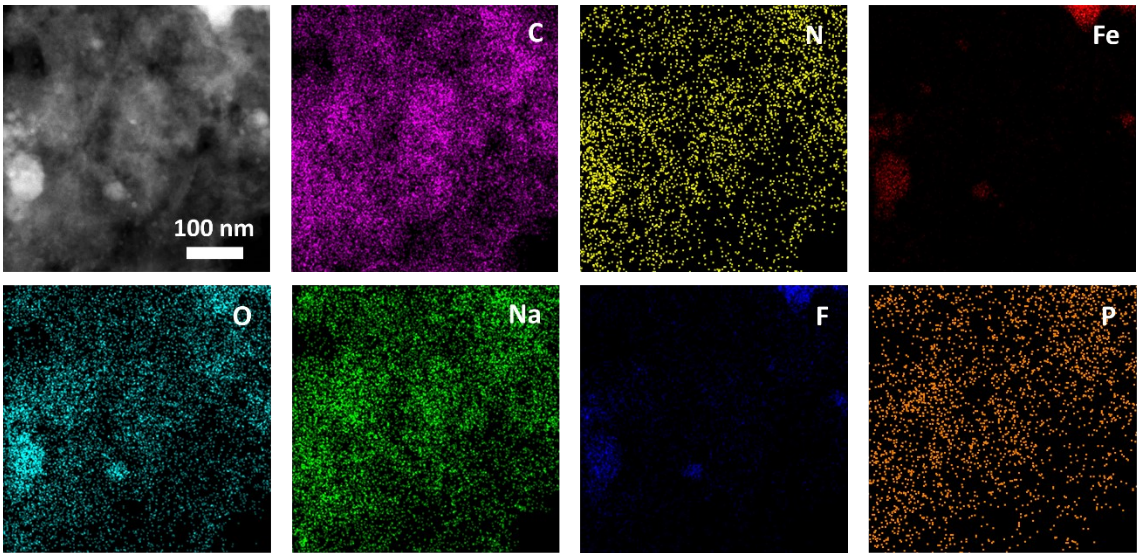

Figure S33. STEM image of SEI layer of FeN_X/C-700 EDS-elemental maps of C, N, Fe, O, Na, F, and P.

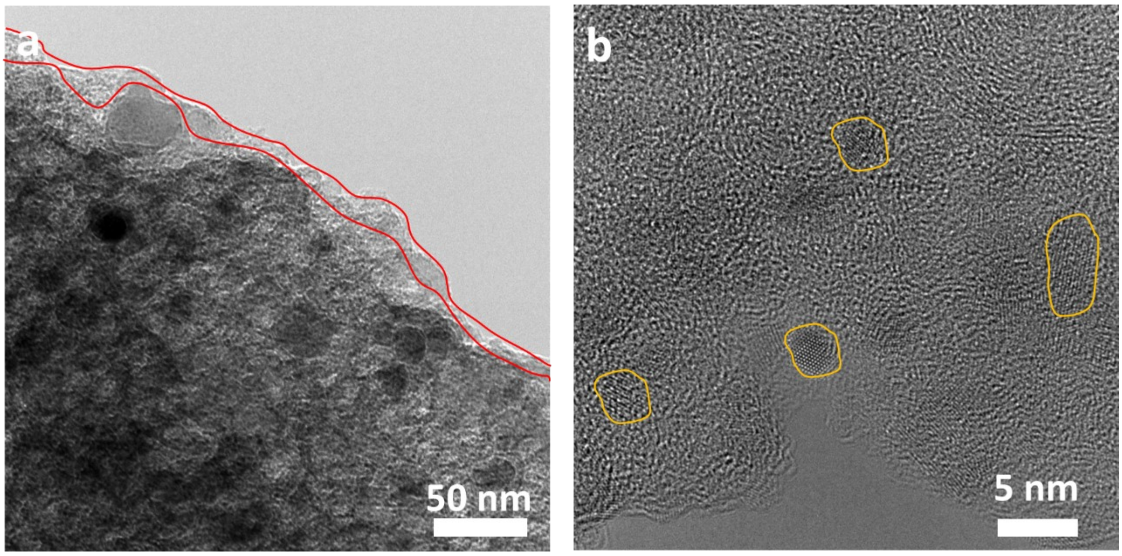

Figure S34. Morphological characterizations of SEI layers, TEM images of FeN_X/C-800 after 10 cycles.

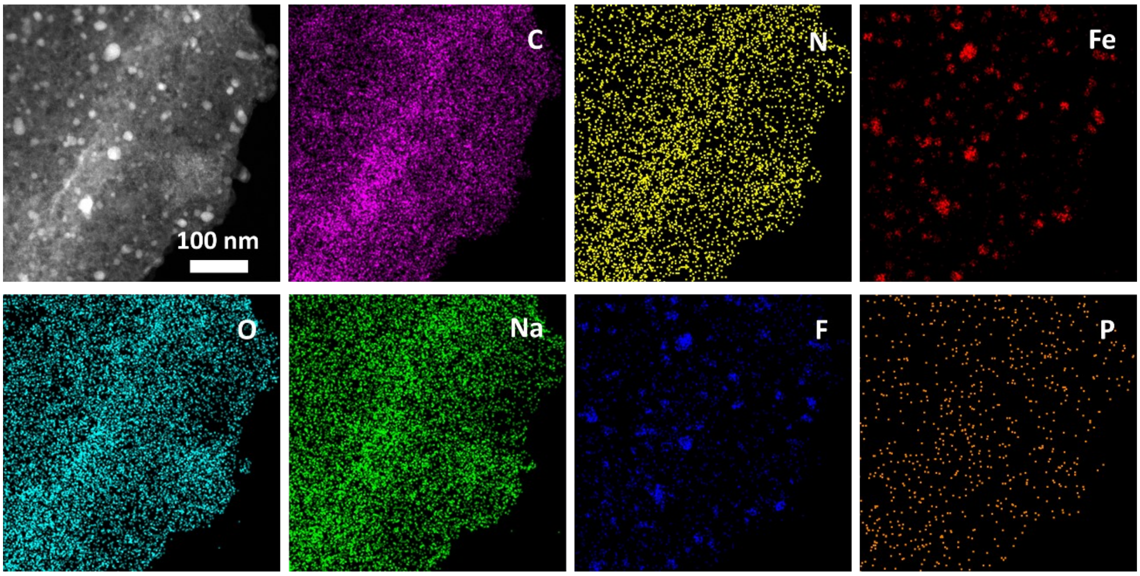

Figure S35. STEM image of SEI layer of FeN_X/C-800 EDS-elemental maps of C, N, Fe, O, Na, F, and P.

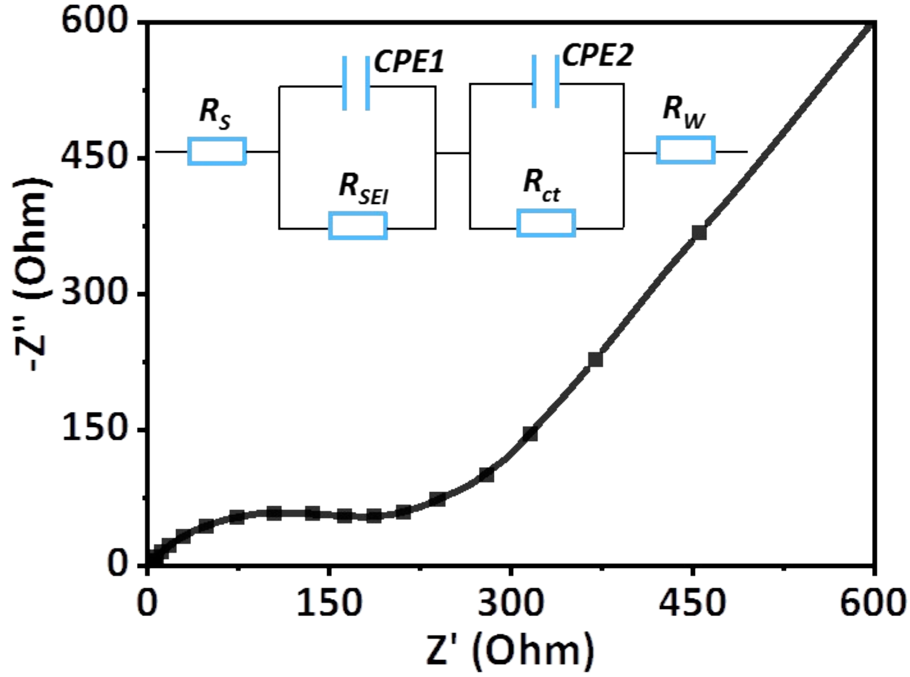

Figure S36. Electrochemical equivalent circuit model for fitting Nyquist plots.

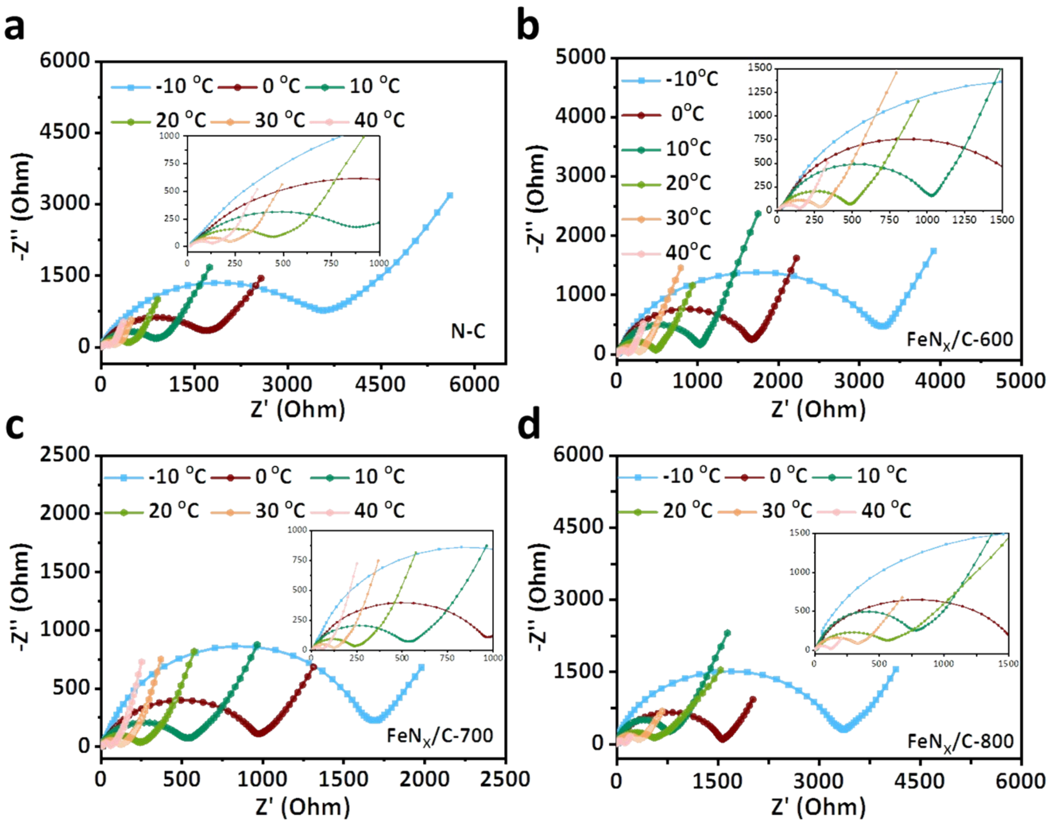

Figure S37. Electrochemical impedance spectroscopy analysis after 10 discharge-charge cycles. Temperature-dependent Nyquist plots of the a) N-C, b) FeN_X/C-600 c) FeN_X/C-700, and d) FeN_X/C-800, respectively.

Table S1. The BET specific surface area and pore volume

Sample	BET (m^2 g^{-1})	Pore volume (cm^3 g^{-1})
FeN_X/C-600	605	0.20
FeN_X/C-700	660	0.29
FeN_X/C-800	352	0.18

Table S2. The different Fe species contents of different samples.

Sample	ICP Fe content (wt%)	FeN area (%)	FeN content (wt%)	Fe_3C area (%)	Fe_3C content (wt%)	Assignment
FeN_X/C-600	2.1	65.29	1.37	34.71	0.73	$Fe^{II}N$ Low spin
FeN_X/C-700	8.0	25.56	2.05	74.44	5.98	$Fe^{II}N$ Low spin
FeN_X/C-800	9.1	2.02	0.18	97.98	8.92	$Fe^{II}N$ Low spin

Table S3. The slope of relationship between log (i) and log (v) for the different samples.

Sample	Anodic	Cathodic
N-C	0.76	0.82
FeNx/C-600	0.92	0.93
FeNx/C-700	0.99	0.99
FeNx/C-800	0.86	0.97

Table S4. The contribution rations of N-C, FeN_X/C-600, FeN_X/C-700, and FeN_X/C-800 at different scanning rates.

Scan rate (mV s^{-1})	N-C		FeN_X/C-600		FeN_X/C-700		FeN_X/C-800	
	Diffusion	Capacitive	Diffusion	Capacitive	Diffusion	Capacitive	Diffusion	Capacitive
0.1	75.9	24.1	56.8	43.2	51.5	48.5	68.1	31.9
0.2	68.7	31.3	52.8	47.2	38.9	61.1	55.6	44.4
0.5	65.4	34.6	46.4	53.6	35.7	64.3	49.7	50.3
1.0	58.8	41.2	37.3	62.7	29.4	70.6	42.2	57.8
2.0	50.6	49.4	29.3	70.7	24.9	75.1	34.3	65.7
5.0	36.8	63.2	18.0	82.0	17.2	82.8	24.9	75.1
10.0	22.7	77.3	12.9	87.1	7.9	92.1	15.6	84.6

Table S5. Resistance of the different sample anodes.

Sample	Temperature (°C)	Re	Rct	RSEI
N-C	-10	20.2	3200	375
	0	19.9	1600	350
	10	20.1	800	300
	20	19.5	450	275
	30	18.7	250	150
	40	18.5	125	60
FeN_x/C-600	-10	22.2	3050	310
	0	16.0	1500	290
	10	15.3	700	200
	20	14.5	300	125
	30	13.5	200	75
	40	11.7	100	50
FeN_x/C-700	-10	16.3	1500	130
	0	13.4	800	110
	10	10.9	300	90
	20	9.9	150	70
	30	9.1	70	50
	40	8.6	50	30
FeN_x/C-800	-10	19.6	3000	350
	0	14.5	1200	300
	10	12.2	600	275
	20	11.1	275	200
	30	10.3	175	125
	40	8.7	75	50